



**HAL**  
open science

## Detection of Dimethyl Ether in the Central Region of the MWC 480 Protoplanetary Disk

Yoshihide Yamato, Yuri Aikawa, Viviana V. Guzmán, Kenji Furuya, Shota Notsu, Gianni Cataldi, Karin I. Öberg, Chunhua Qi, Charles J. Law, Jane Huang, et al.

► **To cite this version:**

Yoshihide Yamato, Yuri Aikawa, Viviana V. Guzmán, Kenji Furuya, Shota Notsu, et al.. Detection of Dimethyl Ether in the Central Region of the MWC 480 Protoplanetary Disk. *The Astrophysical Journal*, 2024, 974, 10.3847/1538-4357/ad6981 . insu-04836801

**HAL Id: insu-04836801**

**<https://insu.hal.science/insu-04836801v1>**

Submitted on 15 Dec 2024

**HAL** is a multi-disciplinary open access archive for the deposit and dissemination of scientific research documents, whether they are published or not. The documents may come from teaching and research institutions in France or abroad, or from public or private research centers.

L'archive ouverte pluridisciplinaire **HAL**, est destinée au dépôt et à la diffusion de documents scientifiques de niveau recherche, publiés ou non, émanant des établissements d'enseignement et de recherche français ou étrangers, des laboratoires publics ou privés.



Distributed under a Creative Commons Attribution 4.0 International License



# Detection of Dimethyl Ether in the Central Region of the MWC 480 Protoplanetary Disk

Yoshihide Yamato<sup>1</sup>, Yuri Aikawa<sup>1</sup>, Viviana V. Guzmán<sup>2</sup>, Kenji Furuya<sup>1,3</sup>, Shota Notsu<sup>4,1,5</sup>, Gianni Cataldi<sup>3</sup>, Karin I. Öberg<sup>6</sup>, Chunhua Qi<sup>6</sup>, Charles J. Law<sup>7,12</sup>, Jane Huang<sup>8</sup>, Richard Teague<sup>9</sup>, and Romane Le Gal<sup>10,11</sup><sup>1</sup> Department of Astronomy, Graduate School of Science, The University of Tokyo, 7-3-1 Hongo, Bunkyo-ku, Tokyo 113-0033, Japan; [yyamato.as@gmail.com](mailto:yyamato.as@gmail.com)<sup>2</sup> Instituto de Astrofísica, Pontificia Universidad Católica de Chile, Av. Vicuña Mackenna 4860, 7820436 Macul, Santiago, Chile<sup>3</sup> National Astronomical Observatory of Japan, Osawa 2-21-1, Mitaka, Tokyo 181-8588, Japan<sup>4</sup> Department of Earth and Planetary Science, Graduate School of Science, The University of Tokyo, 7-3-1 Hongo, Bunkyo-ku, Tokyo 113-0033, Japan<sup>5</sup> Star and Planet Formation Laboratory, RIKEN Cluster for Pioneering Research, 2-1 Hirosawa, Wako, Saitama 351-0198, Japan<sup>6</sup> Center for Astrophysics—Harvard & Smithsonian, 60 Garden Street, Cambridge, MA 02138, USA<sup>7</sup> Department of Astronomy, University of Virginia, Charlottesville, VA 22904, USA<sup>8</sup> Department of Astronomy, Columbia University, 538 W. 120th Street, Pupin Hall, New York, NY, 10027, USA<sup>9</sup> Department of Earth, Atmospheric, and Planetary Sciences, Massachusetts Institute of Technology, Cambridge, MA 02139, USA<sup>10</sup> Institut de Planétologie et d'Astrophysique de Grenoble (IPAG), Université Grenoble Alpes, CNRS, 38000 Grenoble, France<sup>11</sup> Institut de Radioastronomie Millimétrique (IRAM), 38406 Saint-Martin d'Hères, France

Received 2024 June 18; revised 2024 July 28; accepted 2024 July 29; published 2024 October 7

## Abstract

Characterizing the chemistry of complex organic molecules (COMs) at the epoch of planet formation provides insights into the chemical evolution of the interstellar medium (ISM) and the origin of organic materials in our solar system. We report a detection of dimethyl ether ( $\text{CH}_3\text{OCH}_3$ ) in the disk around the Herbig Ae star MWC 480 with sensitive Atacama Large Millimeter/submillimeter Array observations. This is the first detection of  $\text{CH}_3\text{OCH}_3$  in a nontransitional Class II disk. The spatially unresolved, compact ( $\lesssim 25$  au in radius) nature, broad line width ( $\sim 30$  km s<sup>-1</sup>), and high excitation temperature ( $\sim 200$  K) indicate the sublimation of COMs in the warm inner disk. Despite the detection of  $\text{CH}_3\text{OCH}_3$ , methanol ( $\text{CH}_3\text{OH}$ ), the most abundant COM in the ISM, has not been detected, from which we constrain the column density ratio of  $\text{CH}_3\text{OCH}_3/\text{CH}_3\text{OH} \gtrsim 7$ . This high ratio may indicate the reprocessing of COMs during the disk phase, as well as the effect of the physical structure in the inner disk. We also find that this ratio is higher than in COM-rich transition disks recently discovered. This may indicate that in the full disk of MWC 480, COMs have experienced substantial chemical reprocessing in the innermost region, while the COM emission in the transition disks predominantly traces the inherited ice sublimating at the dust cavity edge located at larger radii ( $\gtrsim 20$  au).

*Unified Astronomy Thesaurus concepts:* [Interstellar medium \(847\)](#); [Protoplanetary disks \(1300\)](#); [Astrochemistry \(75\)](#)

## 1. Introduction

Complex organic molecules (COMs), defined empirically as carbon-bearing molecules with six or more atoms, serve as precursors of prebiotic molecules and thus provide insights into the origin of organic materials and life in our solar system (e.g., Ceccarelli et al. 2023). COMs are formed initially on the cold grain surfaces in dark clouds (e.g., Herbst & van Dishoeck 2009) and will be readily observable at radio wavelengths in the warm ( $\gtrsim 100$  K) environment, where they are released into the gas phase by thermal desorption. Indeed, observations with the Atacama Large Millimeter/submillimeter Array (ALMA) have detected a number of COMs in the warm inner envelopes around protostars (e.g., Jørgensen et al. 2018; Belloche et al. 2020; Yang et al. 2021) and the warm protostellar disk around the FU Ori–type outbursting star V883 Ori (van 't Hoff et al. 2018; Lee et al. 2019; Yamato et al. 2024). COMs have also been detected in solar system comets, for example, 67P/Churyumov-Gerasimenko, which has been extensively studied by the Rosetta mission (Altwegg et al. 2019). While comparative studies of COM abundance ratios

suggest that COMs in comets are at least partially inherited from the interstellar medium (ISM; Drozdovskaya et al. 2019), characterizing the distributions and abundances of COMs in protoplanetary disks is crucial for understanding the chemical evolution from the ISM to planetary systems.

Recent sensitive observations with ALMA have revealed the presence of thermally desorbed oxygen-bearing COMs in a few warm transition disks around Herbig Ae stars. van der Marel et al. (2021) detected warm methanol ( $\text{CH}_3\text{OH}$ ) gas localized at the asymmetric dust trap in the transition disk around IRS 48, followed by additional detections in the transition disks of HD 100546 and HD 169142 (Booth et al. 2021b, 2023). IRS 48 exhibits the highest chemical complexity among these disks, where dimethyl ether ( $\text{CH}_3\text{OCH}_3$ ), methyl formate ( $\text{CH}_3\text{OCHO}$ ), and ethylene oxide ( $c\text{-H}_2\text{COCH}_2$ ) have been detected in addition to  $\text{CH}_3\text{OH}$  (Brunken et al. 2022; Booth et al. 2024b). Other oxygen-bearing molecules—such as  $\text{SO}$ ,  $\text{SO}_2$ , and  $\text{NO}$ —have also been detected at the dust trap, indicating the presence of oxygen-rich gas and a low C/O ratio of  $< 1$  (Booth et al. 2021a; Leemker et al. 2023). HD 100546 also exhibits  $\text{CH}_3\text{OCHO}$  emission, but no  $\text{CH}_3\text{OCH}_3$  and  $c\text{-H}_2\text{COCH}_2$ , possibly suggesting a different reservoir of COMs compared to IRS 48 (Booth et al. 2024a). In these transition disks around Herbig Ae stars, the high luminosity of the central star and the inner dust cavity provide a warmer disk condition, which makes it possible for COMs to sublimate.

<sup>12</sup> NASA Hubble Fellowship Program Sagan Fellow.Original content from this work may be used under the terms of the [Creative Commons Attribution 4.0 licence](#). Any further distribution of this work must maintain attribution to the author(s) and the title of the work, journal citation and DOI.

**Table 1**  
Observational Details

Date	# of Ant.	On-source Int. (min)	PWV (mm)	Baseline (m)	Ang. Res. (arcsec)	MRS (arcsec)	Calibrators	
							Bandpass/Amplitude	Phase
2021.1.00535.S (PI: Y. Yamato)								
2022 Aug 8	42	44	0.7	15–1302	0.2	2.6	J0510+1800	J0438+3004
2022 Aug 9	40	44	0.2	15–1246	0.2	3.0	J0510+1800	J0438+3004
2022 Aug 9	40	44	0.1	15–1261	0.2	3.1	J0510+1800	J0438+3004
2022 Aug 10	42	44	0.4	15–1302	0.2	2.8	J0510+1800	J0438+3004
2022 Aug 10	41	44	0.5	15–1302	0.2	3.1	J0510+1800	J0438+3004
2021.1.00982.S (PI: V. V. Guzman)								
2022 Aug 11	45	40	0.5	15–1302	0.2	2.9	J0510+1800	J0438+3004
2022 Aug 11	44	40	0.5	15–1302	0.2	2.8	J0510+1800	J0438+3004
2022 Aug 14	47	40	0.6	15–1302	0.2	2.8	J0510+1800	J0438+3004

However, the current limited detections of sublimated COMs in transition disks preclude a comparison of the COM reservoir between other Herbig and T Tauri disks. Although weak, extended emission of  $\text{CH}_3\text{OH}$  has been detected in the outer cold region ( $\gtrsim 30$  au) of the nearest T Tauri disk TW Hya, its low abundance relative to  $\text{H}_2$  ( $\sim 10^{-11}$ – $10^{-12}$ ) suggests a nonthermal desorption origin (Walsh et al. 2016). Similar attempts to detect  $\text{CH}_3\text{OH}$  in the disks around Herbig Ae stars HD 163296 and MWC 480 yielded nondetections (HD 163296; Carney et al. 2019) or tentative detections (MWC 480; Loomis et al. 2018a) in the outer cold region. In this paper, we present the first detection of  $\text{CH}_3\text{OCH}_3$  in the MWC 480 protoplanetary disk. MWC 480 is a  $\sim 7$  Myr old (Montesinos et al. 2009) Class II Herbig Ae star with a stellar mass of  $M_* \approx 2.1 M_\odot$  (Simon et al. 2019; Teague et al. 2021) in the Taurus–Auriga star-forming region ( $d \approx 162$  pc; Gaia Collaboration et al. 2018). The MWC 480 disk, which has been observed in the Molecules with ALMA at Planet-forming Scales ALMA Large Program (Öberg et al. 2021), is one of the most extensively studied disks around Herbig Ae stars. The MWC 480 disk exhibits a prominent dust ring at  $\approx 98$  au (Long et al. 2018; Liu et al. 2019; Sierra et al. 2021), and the velocity perturbation observed in CO and its isotopologue emission suggests the presence of a planet at  $\approx 245$  au (Teague et al. 2021; Izquierdo et al. 2023). The outer disk ( $\gtrsim 30$  au) of MWC 480 is characterized by a gas-phase  $\text{C}/\text{O} > 1$  (Bosman et al. 2021a; Jiang et al. 2023) and abundant hydrocarbons and cyanides (Guzmán et al. 2021; Ilee et al. 2021), while the inner disk chemistry is unknown.

We describe the ALMA Band 7 observations in Section 2. We present the detection of  $\text{CH}_3\text{OCH}_3$ , the tentative detection of  $\text{CH}_3\text{OCHO}$ , and the nondetection of  $\text{CH}_3\text{OH}$ , from which we constrain the excitation condition and column densities based on the spectral analysis in Section 3. We discuss the results in Section 4, and finally summarize the study in Section 5.

## 2. Observations

We observed the MWC 480 disk in Band 7 during ALMA Cycle 8 (project code: 2021.1.00535.S; PI: Y. Yamato). Observations were carried out in five execution blocks. Observational details including the observation date, number of antennas, on-source integration time, mean precipitable water vapor (PWV), baseline coverage, angular resolution, maximum recoverable scale (MRS), and calibrator information are summarized in Table 1.

The pipeline calibrations were performed by ALMA staff using the standard ALMA pipeline. Subsequent self-calibration and imaging were performed using the Common Astronomy Software Applications (CASA; CASA Team et al. 2022) version 6.2.1.7. The continuum visibilities were produced by averaging the line-free channels specified by visually inspecting the data cubes delivered from the observatory. The continuum emission peak on the image from each execution block was aligned to a common direction,  $\alpha(\text{ICRS}) = 04^{\text{h}}58^{\text{m}}46^{\text{s}}.279$ ,  $\delta(\text{ICRS}) = +29^{\text{d}}50^{\text{m}}36^{\text{s}}.40$ , which was used as the disk center in the following analysis. Then, five rounds of phase-only self-calibration and one round of amplitude self-calibration were performed, resulting in a signal-to-noise ratio (S/N) increase by a factor of  $\approx 15$ . The solutions were then applied to the entire data set. The continuum emission was finally subtracted from the line visibilities by fitting a first-order polynomial to line-free channels using the CASA task `uvcontsub`.

We focused on the spectral window originally dedicated for continuum acquisition, which covered a frequency range of 298.88–300.75 GHz and had a spectral resolution of 1.1 MHz ( $\approx 1.1 \text{ km s}^{-1}$ ). This spectral window contained a number of  $\text{CH}_3\text{OCH}_3$  and  $\text{CH}_3\text{OCHO}$  transitions. We generated a single image cube for the entire frequency range by imaging the self-calibrated, continuum-subtracted visibilities with a channel spacing of  $4 \text{ km s}^{-1}$  and a Briggs robust value of 0.5, in the modified Briggs weighting scheme of `briggsbw taper` implemented in the `tclean` task. The large channel width of  $4 \text{ km s}^{-1}$  was intended to boost the S/N of the detected  $\text{CH}_3\text{OCH}_3$  emission while resolving its broad line width. The CLEANed image cube has a synthesized beam of  $0''.31 \times 0''.21$  (PA =  $8^\circ 2$ ) and an rms noise level of  $0.33 \text{ mJy beam}^{-1}$  at  $4 \text{ km s}^{-1}$  channel width. The rms noise was measured on the line-free region of the image cube prior to primary beam correction. We also generated the continuum image at 1.03 mm with a Briggs robust value of  $-0.5$  to better resolve the gapping structure, which is shown in the top left panel of Figure 1. Additionally, we report the detection of a new submillimeter source in the same field of view in Appendix D.

We also used the Band 7 data from another project (project code: 2021.1.00982.S; PI: V. V. Guzman). Observations were carried out in three execution blocks and their details are summarized in Table 1. The continuum spectral window of this data set, which is used in this study, covered a frequency range of 288.56–290.43 GHz, with a spectral resolution of 1.1 MHz ( $\approx 1.2 \text{ km s}^{-1}$ ). This spectral window covered a cluster of

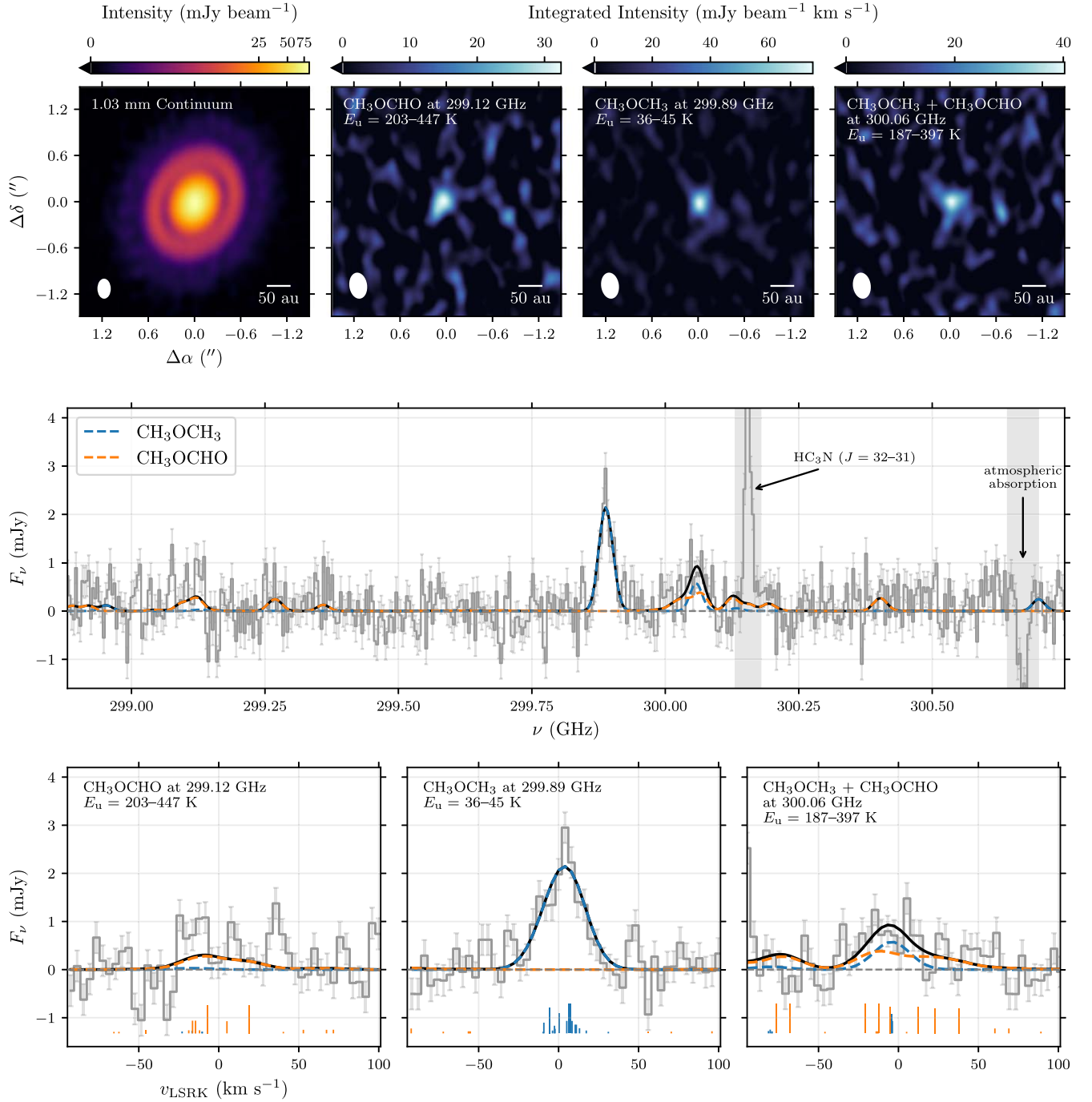


**Figure 1.** Summary of the observations toward the MWC 480 disk. Top: 1.03 mm continuum image (left) and velocity-integrated intensity maps of (tentatively) detected COMs,  $\text{CH}_3\text{OCH}_3$ , and  $\text{CH}_3\text{OCHO}$  (others). The peak S/Ns of the right three maps are 5.4, 12, and 6.0, respectively. The white ellipse in the lower left corner indicates the synthesized beam. A scale bar of 50 au is shown in the lower right corner. Middle: spectra extracted in a circular aperture with  $0''.6$  diameter toward the disk center (gray), overlaid with the best-fit spectral model for  $\text{CH}_3\text{OCH}_3$  (blue),  $\text{CH}_3\text{OCHO}$  (orange), and the sum of both (black). The semitransparent error bars represent the associated  $1\sigma$  uncertainties. The frequency ranges removed from the fit due to the atmospheric absorption or contamination from other molecular lines are shaded in gray. Bottom: zoom-in view of the middle panel in the vicinity of the (tentatively) detected features, but with the spectral axis in velocity with respect to a reference frequency of 299.11170 GHz (left), 299.89209 GHz (middle), and 300.05338 GHz (right), respectively. The vertical line segments at the bottoms of the panels indicate the center and the relative strength (at 200 K) of each transition.

$\text{CH}_3\text{OH}$  transitions, which were used to constrain the upper limit on the  $\text{CH}_3\text{OH}$  column density. We followed the same self-calibration procedure as above, but with CASA version 6.4.1. We performed three rounds of phase-only self-calibration and one round of amplitude self-calibration, which resulted in an increase in S/N by a factor of  $\approx 5.5$ . We generated the image cube of the continuum spectral window in the same manner as above. The

resulting beam size and the rms noise level were  $0''.31 \times 0''.22$  (PA =  $-3^\circ.4$ ) and  $0.67 \text{ mJy beam}^{-1}$  at  $4 \text{ km s}^{-1}$  channel width.

For both data sets, the absolute flux calibration uncertainty is expected to be  $\lesssim 10\%$ , based on the Quality Assurance (QA2) criteria described in the ALMA Cycle 8 Technical Handbook. The following analyses consider only the statistical uncertainty and do not include the systematic flux calibration uncertainty.

**Table 2**  
Results of the Spectral Analysis

Molecule	$T_{\text{ex}}$ (K)	$\Delta V_{\text{FWHM}}$ (km s <sup>-1</sup> )	$v_{\text{sys}}$ (km s <sup>-1</sup> )	$N$ (cm <sup>-2</sup> )	$/N(\text{CH}_3\text{OH})$
CH <sub>3</sub> OCH <sub>3</sub>				$7.4_{-3.2}^{+4.6} \times 10^{15}$	>7
CH <sub>3</sub> OCHO				$7.4_{-4.9}^{+3.6} \times 10^{14}$	>0.81 <sup>a</sup>
CH <sub>3</sub> OH	$200_{-50}^{+50}$	$30_{-6}^{+8}$	$4.3_{-2.5}^{+2.4}$	$<9.1 \times 10^{14}$	...
CH <sub>3</sub> CHO				$<1.9 \times 10^{14}$	...

**Note.**

<sup>a</sup> The median value of  $N(\text{CH}_3\text{OCHO})$  divided by the  $N(\text{CH}_3\text{OH})$  upper limit, which should be viewed as tentative. See Appendix B for details.

### 3. Detection of Dimethyl Ether

#### 3.1. Spectra and Spatial Distributions

We first extracted the integrated spectra by spatially integrating the image cubes in a circular aperture with 0''6 diameter toward the disk center, which securely covers the apparent emission, as shown later. The middle panel of Figure 1 shows the resulting spectrum of the data containing detected CH<sub>3</sub>OCH<sub>3</sub> transitions. We found a clear spectral feature at  $\sim 299.89$  GHz, whose line center spectrally coincides with the rest frequencies of CH<sub>3</sub>OCH<sub>3</sub> transitions, taking into account the spectral shift due to the systemic velocity (5.1 km s<sup>-1</sup>; Piétu et al. 2007; Teague et al. 2021). This feature is a blend of 12 individual CH<sub>3</sub>OCH<sub>3</sub> transitions (see Table 3 in Appendix B for their spectroscopic properties) and shows a peak S/N of 9.4. In addition, two tentative features are seen at  $\sim 299.12$  and  $\sim 300.06$  GHz, which also match with the frequencies of the CH<sub>3</sub>OCH<sub>3</sub> and CH<sub>3</sub>OCHO transitions. These features show peak S/Ns of 3.4 and 4.7, respectively. Because they are lower than the typical detection criteria of  $5\sigma$  and the latter is blended between different species (CH<sub>3</sub>OCH<sub>3</sub> and CH<sub>3</sub>OCHO), these transitions were considered tentative detections. The zoomed-in spectra around these features are presented in the bottom panels of Figure 1, along with the expected spectral locations of the CH<sub>3</sub>OCH<sub>3</sub> and CH<sub>3</sub>OCHO transitions. We note that an exhaustive search for other molecular lines that could be responsible for those features was performed, but only CH<sub>3</sub>OCH<sub>3</sub> and CH<sub>3</sub>OCHO can consistently explain these features among the lines of detectable species/transitions in a typical disk environment.

The velocity-integrated intensity maps of these spectral features, generated using the Python package `bettermoments` (Teague & Foreman-Mackey 2018), with no flux threshold for pixel inclusion, are shown in the top panels of Figure 1, along with the 1.03 mm dust continuum image. These maps show the spatially unresolved, compact emission with a peak S/N of  $\sim 5$ –12.

Several strong transitions of CH<sub>3</sub>OH and CH<sub>3</sub>CHO were covered by the data from the project 2021.1.00982.S (see Table 3 in Appendix B for the covered strong transitions), but they have not been detected in the image plane.

We also verified the (tentative) detections/nondetections of these COMs by matched filter analysis (Loomis et al. 2018b). The details and resulting response spectra are shown in Appendix A. The  $\sim 5\sigma$ – $17\sigma$  responses for CH<sub>3</sub>OCH<sub>3</sub> and CH<sub>3</sub>OCHO signify the detection of them, although it should be noted that the detected features are a blend of multiple transitions.

#### 3.2. Spectral Analysis

To characterize the excitation temperatures and column densities of molecules, we employ a spectral fit with a simple local thermodynamic equilibrium (LTE) slab model. We basically followed the method described in Yamato et al. (2024), which is detailed in Appendix B. Briefly, the entire spectra are modeled with a total of seven free parameters: beam-averaged column densities of four molecular species ( $N(\text{CH}_3\text{OCH}_3)$ ,  $N(\text{CH}_3\text{OCHO})$ ,  $N(\text{CH}_3\text{OH})$ , and  $N(\text{CH}_3\text{CHO})$ ), the excitation temperature  $T_{\text{ex}}$ , which is assumed to be common among different species/transitions, the line width  $\Delta V$  (including the broadening due to disk rotation), and the systemic velocity  $v_{\text{sys}}$ . Although CH<sub>3</sub>OH and CH<sub>3</sub>CHO are not detected, this simultaneous fit allows us to constrain the upper limit on their column densities. The assumption of a common excitation temperature for all COM species reflects the expectation that different COMs sublimate simultaneously with water ice.

We explore the parameter space with the affine-invariant Markov Chain Monte Carlo (MCMC) algorithm implemented in the Python package `emcee` (Foreman-Mackey et al. 2013). The details of this fitting procedure are described in Appendix B. Figure 1 compares the best-fit model with the observed spectra. The three observed spectral features are well reproduced by the best-fit model. While the robust feature at  $\sim 299.89$  GHz is explained by the cluster of CH<sub>3</sub>OCH<sub>3</sub> transitions with relatively low upper-state energies of 36–45 K, two other tentative features correspond to the transitions of CH<sub>3</sub>OCH<sub>3</sub> and CH<sub>3</sub>OCHO, with higher upper-state energies of 187–447 K (see Table 3). The result of the fit is summarized in Table 2. The excitation temperature and line width are constrained to be  $T_{\text{ex}} = 200_{-50}^{+50}$  K and  $\Delta V = 30_{-6}^{+8}$  km s<sup>-1</sup>, where the uncertainties are 16th and 84th percentiles (corresponding to  $1\sigma$ ) of the posterior distributions. The resulting beam-averaged column densities of CH<sub>3</sub>OCH<sub>3</sub> and CH<sub>3</sub>OCHO are  $7.4_{-3.2}^{+4.6} \times 10^{15}$  and  $7.4_{-4.9}^{+3.6} \times 10^{14}$  cm<sup>-2</sup>, respectively. The upper limits on the column densities of CH<sub>3</sub>OH and CH<sub>3</sub>CHO are also constrained to be  $<9.1 \times 10^{14}$  and  $<1.9 \times 10^{14}$  cm<sup>-2</sup>, respectively. These upper limits are the 99.85th percentile (corresponding to  $3\sigma$ ) of the posterior distributions. From these constraints on column densities, we derive a CH<sub>3</sub>OCH<sub>3</sub>/CH<sub>3</sub>OH column density ratio (lower limit) of >7.

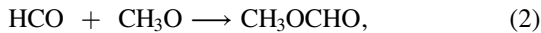
## 4. Discussion

#### 4.1. Chemical Origin of the COM Emission

The spatially unresolved, compact ( $\lesssim 25$  au radius) CH<sub>3</sub>OCH<sub>3</sub> emission with a broad line width ( $\sim 30$  km s<sup>-1</sup>) and a high excitation temperature ( $\sim 200$  K; see Section 3.2) indicates warm CH<sub>3</sub>OCH<sub>3</sub> gas in the inner disk. This is the first observational

evidence of COMs sublimated in the inner warm region of the MWC 480 disk. The observed broad line width is also reproduced with the emission originating from  $\lesssim 20$  to 30 au radii, where the disk temperature is  $\gtrsim 80$ –100 K, by a more detailed radiative transfer calculation (see Appendix C), further supporting this interpretation. Indeed, the peak brightness temperature of the CO  $J=2-1$  emission already reaches  $\gtrsim 70$  K at  $\approx 50$  au (Law et al. 2021), implying that the inner disk of MWC 480 is warm enough ( $\gtrsim 100$  K) for COMs to sublimate. Furthermore, a super-resolution image of the Band 6 continuum emission shows a steep brightness increase inside a 20 au radius (Yamaguchi et al. 2024), potentially suggesting the sublimation of water and COMs there that modify the dust optical properties. As the (sub)millimeter dust continuum emission from the midplane is optically thick in the inner  $\lesssim 40$  au (Sierra et al. 2021), the observed  $\text{CH}_3\text{OCH}_3$  emission likely traces the disk surface layer.

The  $\text{CH}_3\text{OCH}_3$  detection and its icy origin lead us to expect the detection of other COMs, particularly the most abundant COM in the ISM,  $\text{CH}_3\text{OH}$ . However, the  $\text{CH}_3\text{OH}$  transitions ( $E_u \gtrsim 40$  K) have not been detected in the present observations, resulting in a high  $\text{CH}_3\text{OCH}_3/\text{CH}_3\text{OH}$  column density ratio of  $>7$  (Section 3.2). This value is considerably higher than the typical values in the warm inner envelopes around protostars (e.g., Jørgensen et al. 2018; Yang et al. 2021), by more than 1 order of magnitude. This may indicate the efficient formation of  $\text{CH}_3\text{OCH}_3$  during the disk phase. While it is anticipated that  $\text{CH}_3\text{OH}$  predominantly forms via hydrogenation of CO on the cold grain surfaces in the dark cloud (e.g., Watanabe & Kouchi 2002), more complex species, such as  $\text{CH}_3\text{OCH}_3$  and  $\text{CH}_3\text{OCHO}$ , may also form on the grain surface in situ in disks. Disk chemical models suggest that radical–radical reactions on the warm ( $\sim 30$ –50 K) grain surfaces may enhance the abundance of  $\text{CH}_3\text{OCH}_3$  and  $\text{CH}_3\text{OCHO}$  (e.g., Furuya & Aikawa 2014):



where the ingredient radicals ( $\text{CH}_3$ ,  $\text{CH}_3\text{O}$ , and  $\text{HCO}$ ) are the photodissociation products of  $\text{CH}_3\text{OH}$  ice (Öberg et al. 2009). These reactions, triggered by energetic processes such as UV, X-rays, and cosmic rays, will play a pivotal role in determining the abundance of COMs during the disk phase. Additionally, gas-phase formation in the inner warm region may also be a contributing factor, as suggested by astrochemical models (Taquet et al. 2016; Garrod et al. 2022).

The derived column density ratio ( $\text{CH}_3\text{OCH}_3/\text{CH}_3\text{OH} > 7$ ) is still higher than the prediction of those models, which is lower than unity (e.g., Furuya & Aikawa 2014; Taquet et al. 2016). This implies that some additional effect is necessary to explain the observations. One possibility is the difference in the distributions between  $\text{CH}_3\text{OCH}_3$  and  $\text{CH}_3\text{OH}$ . The slightly higher binding energy of  $\text{CH}_3\text{OH}$  ( $\approx 5000$ –6600 K; Ferrero et al. 2020; Minissale et al. 2022) than of  $\text{CH}_3\text{OCH}_3$  ( $\approx 4000$ –6500 K; Ligterink & Minissale 2023) may cause the  $\text{CH}_3\text{OH}$  ice to sublimate in warmer regions (i.e., smaller radii) and the  $\text{CH}_3\text{OH}$  emission to be more heavily beam-diluted (see Appendix C for a test of this possibility). Additionally, dust continuum emission may selectively hide the  $\text{CH}_3\text{OH}$  emission that could originate from a more inner region (e.g., Bosman et al. 2021b; Yamato et al. 2024).

Taken together, we suggest that the substantial reprocessing of COMs during the disk phase, in conjunction with an additional effect of the difference in spatial distributions, could explain the detection of  $\text{CH}_3\text{OCH}_3$  but not  $\text{CH}_3\text{OH}$ . Further

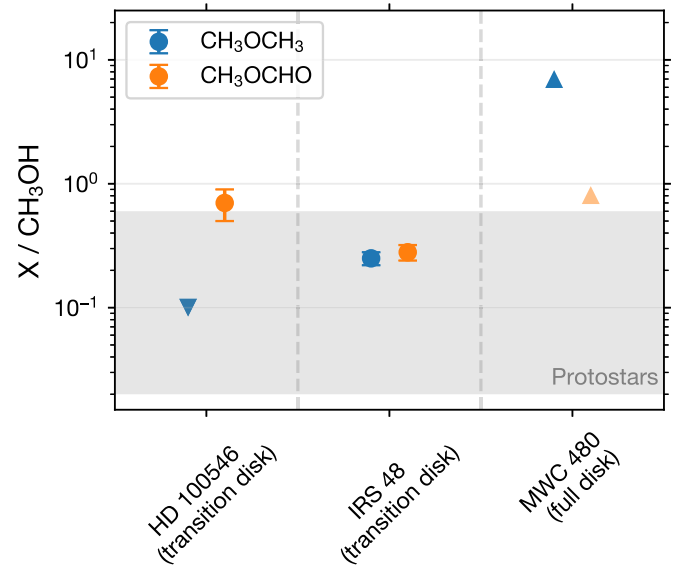


**Figure 2.** Comparison of the column density ratios of  $\text{CH}_3\text{OCH}_3$  and  $\text{CH}_3\text{OCHO}$  relative to  $\text{CH}_3\text{OH}$  in three disks: HD 100546 (Booth et al. 2024a), Oph IRS 48 (Booth et al. 2024b), and MWC 480 (this work). The upward and downward triangles indicate lower and upper limits, respectively. Given the tentative detection (see Section 3.2), the value of  $\text{CH}_3\text{OCHO}$  in MWC 480 is plotted with transparency. The shaded region indicates the typical range of protostellar values measured by extensive line surveys (PILS—Jørgensen et al. 2016; CALYPSO—Belloche et al. 2020; PEACHES—Yang et al. 2021).

observations at higher resolution and sensitivity are required to more accurately constrain the distributions and abundance ratio of COMs, thus enabling a better inference of the reprocessing of COMs during the disk phase.

## 4.2. Comparison to other Disks

### 4.2.1. COM-rich Transition Disks

Recent deep-line surveys have identified the emission from the warm gas of sublimated COMs in three transition disks: HD 100546, Oph IRS 48, and HD 169142 (Booth et al. 2023, 2024a, 2024b). Multiple species have been detected in Oph IRS 48 ( $\text{CH}_3\text{OH}$ ,  $\text{CH}_3\text{OCH}_3$ ,  $\text{CH}_3\text{OCHO}$ , and  $c\text{-H}_2\text{COCH}_2$ ) and HD 100546 ( $\text{CH}_3\text{OH}$  and  $\text{CH}_3\text{OCHO}$ ), while only  $\text{CH}_3\text{OH}$  has been detected in HD 169142. On the other hand, in full disks, no previous detections of sublimated COMs have been reported, and the present study provides the first evidence of icy organic sublimates. Figure 2 compares the abundance ratios of  $\text{CH}_3\text{OCH}_3$  and  $\text{CH}_3\text{OCHO}$  relative to  $\text{CH}_3\text{OH}$  among HD 100546 (Booth et al. 2024a), Oph IRS 48 (Booth et al. 2024b), and MWC 480. The abundance ratios exhibit a considerable degree of variability among the sources, with particularly elevated values in the full disk of MWC 480. This suggests the potentially different chemistry and/or the effect of varying physical structures between transition and full disks. The abundance ratios in these transition disks may be determined predominantly by the sublimation of inherited ices at the dust cavity edge (or dust trap) located at larger radii ( $\gtrsim 20$  au; e.g., Booth et al. 2021b). In contrast, in the full disk of MWC 480, COM emission is likely to originate from more inner regions ( $\lesssim 20$ –30 au), where COMs may have experienced more reprocessing by, e.g., X-ray-driven chemistry and/or gas-phase chemistry in the disk surface layer. Indeed, the higher fractional abundance of  $\text{HCO}^+$  relative to CO in MWC 480 compared to HD 100546 and IRS 48 may indicate a

higher X-ray flux (Aikawa et al. 2021; Booth et al. 2024a, 2024b), although the lower  $\text{HCO}^+$  abundance in HD 100546 and IRS 48 could be attributed to the presence of gas-phase  $\text{H}_2\text{O}$  that destroys  $\text{HCO}^+$  (e.g., Leemker et al. 2021).

It should also be noted that we obtain a tight upper limit on the  $\text{CH}_3\text{CHO}$  column density, which is less than  $\sim 3\%$  of the  $\text{CH}_3\text{OCH}_3$  column. This is in a similar trend to the nondetection of  $\text{CH}_3\text{CHO}$  in the IRS 48 and HD 100546 disks (Booth et al. 2024a, 2024b), while in contrast to the protostellar envelopes/disks where  $\text{CH}_3\text{CHO}$  exists in a comparable amount of  $\text{CH}_3\text{OCH}_3$  (e.g., Jørgensen et al. 2018; Yang et al. 2021; Yamato et al. 2024). This might indicate that the specific reactions and/or branching ratios that are relevant to  $\text{CH}_3\text{CHO}$  formation/destruction may be at work in the disk phase, as suggested by the detection of  $c\text{-H}_2\text{COCH}_2$ , the isomer of  $\text{CH}_3\text{CHO}$ , in IRS 48 (Booth et al. 2024b).

#### 4.2.2. Nondetection in HD 163296

It is also noteworthy that the same transitions of  $\text{CH}_3\text{OCH}_3$  toward another well-studied full disk around the Herbig Ae star HD 163296 have not been detected with a similar sensitivity and resolution in the same project.<sup>13</sup> This suggests that the chemistry and/or physical structure in the inner disk may be different between MWC 480 and HD 163296. The CO snowline in MWC 480 is located at a larger radius ( $\sim 100$  au) than in HD 163296 ( $\sim 65$  au), as demonstrated in a comprehensive thermochemical modeling study (Zhang et al. 2021), implying a warmer inner disk of MWC 480. The higher rotation temperature of the  $\text{HC}_3\text{N}$  emission in the inner  $\lesssim 10$  au ( $\sim 90$  K versus  $\sim 60$  K) may also indicate that the inner region is warmer in MWC 480 (Ilee et al. 2021). Furthermore, the slightly higher mass accretion rate and bolometric luminosity of MWC 480 (Montesinos et al. 2009; Mendigutía et al. 2013; Fairlamb et al. 2015) may result in a greater quantity of organics being delivered to the inner disk (e.g., Banzatti et al. 2023).

## 5. Summary and Conclusion

We present ALMA Band 7 observations toward the disk around the Herbig Ae star MWC 480. We detected the line emission of  $\text{CH}_3\text{OCH}_3$  and tentatively detected  $\text{CH}_3\text{OCHO}$  for the first time in the MWC 480 disk. This is the first detection of  $\text{CH}_3\text{OCH}_3$  in a nontransitional Class II disk. The compact, spatially unresolved nature at a resolution of  $\sim 0''.3$  (or  $\sim 25$  au radius), the broad line width ( $\sim 30 \text{ km s}^{-1}$  in FWHM), and the high excitation temperature ( $\sim 200$  K) indicate ice sublimation in the warm inner disk.

Furthermore, we present a nondetection of  $\text{CH}_3\text{OH}$ , which results in a high  $\text{CH}_3\text{OCH}_3/\text{CH}_3\text{OH}$  column density ratio of  $>7$ . This high ratio may be explained by the efficient formation of  $\text{CH}_3\text{OCH}_3$  during the disk phase, triggered by UV, X-ray, and cosmic rays, with a possible difference in the spatial distributions between  $\text{CH}_3\text{OCH}_3$  and  $\text{CH}_3\text{OH}$ . We compare the column density ratios of COMs with those in COM-rich transition disks that have recently been discovered. The higher ratios in the full disk of MWC 480 may point to substantial chemical reprocessing of COMs in the innermost region, while

those in transition disks may predominantly trace the sublimation of inherited ice at the dust trap located at  $\gtrsim 20$  au.

The detection of  $\text{CH}_3\text{OCH}_3$  in MWC 480 provides the first evidence of icy organic sublimates in a full disk. Further observations, including the confirmation of the detection with other transitions, and detailed disk chemical modeling are necessary to better understand the inner disk chemistry. In particular, future JWST observations will provide complementary information about the COM abundances in gas and solid phases, which can be compared with the gas-phase abundances estimated from ALMA observations.

## Acknowledgments

We thank the anonymous referee for constructive comments that improved the manuscript. This paper makes use of the following ALMA data: ADS/JAO.ALMA#2021.1.00535.S and ADS/JAO.ALMA#2021.1.00982.S. ALMA is a partnership of ESO (representing its member states), NSF (USA) and NINS (Japan), together with NRC (Canada), NSTC and ASIAA (Taiwan), and KASI (Republic of Korea), in cooperation with the Republic of Chile. The Joint ALMA Observatory is operated by ESO, AUI/NRAO, and NAOJ. The National Radio Astronomy Observatory is a facility of the National Science Foundation operated under cooperative agreement by Associated Universities, Inc. Y.Y. acknowledges support by a Grant-in-Aid for the Japan Society for the Promotion of Science (JSPS) Fellows (KAKENHI grant No. JP23KJ0636). Y.A. acknowledges support by MEXT/JSPS Grants-in-Aid for Scientific Research (KAKENHI) grant Nos. JP20H05847, JP21H04495, and JP24K00674 and NAOJ ALMA Scientific Research grant code 2019-13B. V.V.G. gratefully acknowledges support from FONDECYT Regular 1221352 and ANID CATA-BASAL project FB210003. K.F. acknowledges support by MEXT/JSPS Grants-in-Aid for Scientific Research (KAKENHI) grant No. JP21K13967. S.N. is grateful for support from Grants-in-Aid for JSPS (Japan Society for the Promotion of Science) Fellows grant No. JP23KJ0329 and MEXT/JSPS Grants-in-Aid for Scientific Research (KAKENHI) grant Nos. JP20K22376, JP23K13155, JP20H05845, and JP23H05441. Support for C.J.L. was provided by NASA through the NASA Hubble Fellowship grant No. HST-HF2-51535.001-A awarded by the Space Telescope Science Institute, which is operated by the Association of Universities for Research in Astronomy, Inc., for NASA, under contract NAS5-26555.

*Facility:* ALMA.

*Software:* CASA (CASA Team et al. 2022), bettermoments (Teague & Foreman-Mackey 2018), VISIBLE (Loomis et al. 2018b), keplerian\_mask.py (Teague 2020), emcee (Foreman-Mackey et al. 2013), corner.py (Foreman-Mackey 2016), RADMC-3D (Dullemond et al. 2012), Numpy (Harris et al. 2020), Scipy (Virtanen et al. 2020), Matplotlib (Hunter 2007), Astropy (Astropy Collaboration et al. 2013, 2018, 2022), cmocean (Thyng et al. 2016).

## Appendix A Matched Filter Analysis

We performed the matched filter analysis (Loomis et al. 2018b), which is commonly used to extract weak molecular line emission in protoplanetary disks, to verify the detections/nondetections of COMs. As a filter kernel, we used a simple Keplerian rotating disk model generated with the Python script keplerian\_mask (Teague 2020), assuming a disk inclination

<sup>13</sup> It should be noted that the physical scales traced by these observations are slightly different between MWC 480 and HD 163296, since the angular resolutions ( $\sim 0''.3$ ) are the same but the distances are different (162 pc versus 101 pc).

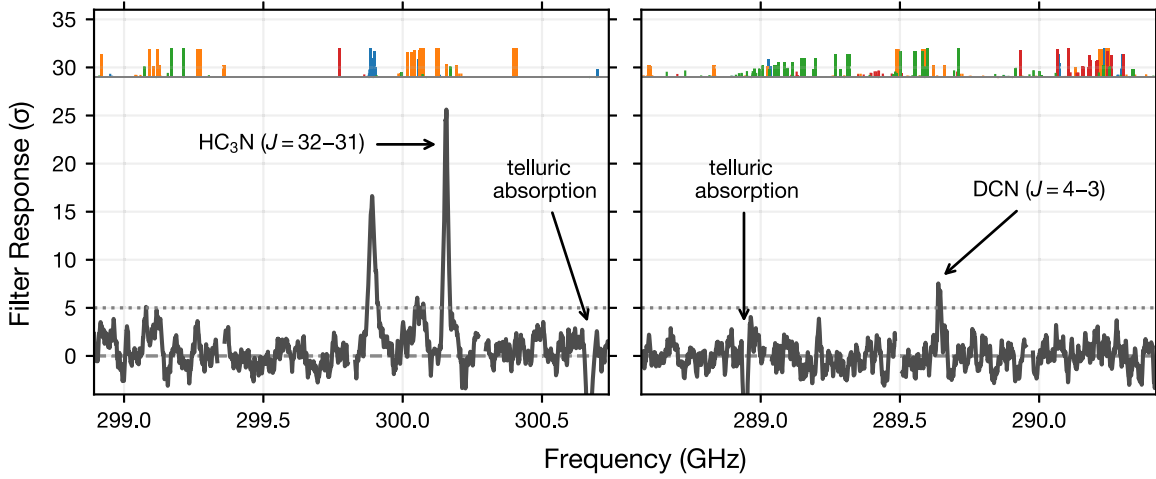


**Figure 3.** Matched filter responses. The horizontal dotted line marks  $5\sigma$ . The relative intensities of the covered lines at 200 K are shown by the vertical segments for  $\text{CH}_3\text{OCH}_3$  (blue),  $\text{CH}_3\text{OCHO}$  (orange),  $\text{CH}_3\text{OH}$  (red), and  $\text{CH}_3\text{CHO}$  (green). A cluster of  $\text{CH}_3\text{OCH}_3$  lines at  $\sim 299.89$  GHz exhibits a  $\sim 17\sigma$  response, while the tentative features at  $\sim 299.12$  GHz and  $\sim 300.06$  GHz show  $\sim 5\sigma$ – $6\sigma$  responses.

angle of  $37^\circ 0$ , position angle of  $148^\circ 0$ , and central stellar mass of  $2.1 M_\odot$  (Öberg et al. 2021; Teague et al. 2021). The outer radius of the disk was set as  $0'' 15$ , based on the extent of the emission in the velocity-integrated intensity maps. The Python package `VISIBLE` (Loomis et al. 2018b) was used to compute the cross-correlation between the observed visibilities and the filter kernel. The resultant response spectra are shown in Figure 3. The brightest cluster of  $\text{CH}_3\text{OCH}_3$  lines at  $\sim 299.89$  GHz shows a  $\sim 17\sigma$  filter response, while the two tentative features at  $\sim 299.12$  GHz and  $\sim 300.06$  GHz exhibit  $\sim 5\sigma$ – $6\sigma$  filter responses. The response spectra do not exhibit any  $\geq 5\sigma$  responses of  $\text{CH}_3\text{OH}$  and  $\text{CH}_3\text{CHO}$  transitions.

## Appendix B Details of Spectral Analysis

Here, we describe the details of the spectral analysis (Section 3.2) for deriving the excitation temperature and column density of COMs. We fit the entire spectra with an LTE slab model based on the basic radiative transfer equations (e.g., Yamato et al. 2024). The emergent intensity of the line emission  $I_\nu$  at each frequency is modeled as

$$I_\nu = (B_\nu(T_{\text{ex}}) - B_\nu(T_{\text{CMB}}))(1 - e^{-\tau_\nu}), \quad (\text{B1})$$

where  $B_\nu$  is the Planck function of the blackbody radiation,  $T_{\text{ex}}$  is the excitation temperature,  $T_{\text{CMB}} = 2.73$  K is the temperature of the cosmic microwave background, and  $\tau_\nu$  is the optical depth profile. We assume that  $T_{\text{ex}}$  is shared by different species of COMs, i.e., the emitting regions are common among different COMs, given that COMs are expected to sublimate at a similar temperature. The optical depth profile  $\tau_\nu$  is computed as

$$\tau_\nu = \sum_i \frac{c^2 A_{ul,i} N_{u,i}}{8\pi\nu^2} \left[ \exp\left(\frac{h\nu}{k_B T_{\text{ex}}}\right) - 1 \right] \phi_{\nu,i}, \quad (\text{B2})$$

where  $c$  is the speed of light,  $A_{ul,i}$  is the Einstein A coefficient of the  $i$ th transition,  $N_{u,i}$  is the upper-state column density of the  $i$ th transition,  $h$  is the Planck constant,  $k_B$  is the Boltzmann constant, and  $\phi_{\nu,i}$  is the line profile function of the  $i$ th transition. The summation  $i$  goes over different transitions of all molecular species. The upper-state column density  $N_{u,i}$  is related to the

total column density  $N$  as

$$N_{u,i} = \frac{N}{Q(T_{\text{ex}})} g_{u,i} \exp\left(-\frac{E_{u,i}}{k_B T_{\text{ex}}}\right), \quad (\text{B3})$$

where  $Q$  is the partition function,  $g_u$  is the upper-state degeneracy, and  $E_u$  is the upper-state energy. The line profile function  $\phi_{\nu,i}$  in Equation (B2) is defined as

$$\phi_{\nu,i} = \frac{1}{\sqrt{2\pi} \sigma_{\nu,i}} \exp\left[-\frac{(\nu - \nu_{0,i} - \delta\nu_i)^2}{2\sigma_{\nu,i}^2}\right], \quad (\text{B4})$$

where  $\sigma_{\nu,i}$  is the frequency line width,  $\nu_{0,i}$  is the rest frequency of the  $i$ th transition, and  $\delta\nu_i$  is the frequency shift due to the systemic velocity  $v_{\text{sys}}$ . The frequency line width  $\sigma_{\nu,i}$  is related to the velocity line width in FWHM  $\Delta V_{\text{FWHM}}$  as  $\sigma_{\nu,i} = \frac{\nu_{0,i} \Delta V_{\text{FWHM}}}{c \sqrt{8 \ln 2}}$ .<sup>14</sup>

Within this model, we consider  $>600$  transitions of four molecular species— $\text{CH}_3\text{OCH}_3$ ,  $\text{CH}_3\text{OCHO}$ ,  $\text{CH}_3\text{OH}$ , and  $\text{CH}_3\text{CHO}$ —whose Einstein A coefficient is larger than  $10^{-8} \text{ s}^{-1}$  and upper-state energy is lower than 1000 K. Table 3 lists the strong transitions and their spectroscopic properties that effectively constrain the column density (and its upper limit). The spectroscopic data of these transitions, including partition functions, are taken from the Cologne Database for Molecular Spectroscopy (Müller et al. 2001, 2005; Endres et al. 2016) for  $\text{CH}_3\text{OCH}_3$  and  $\text{CH}_3\text{OH}$  and the Jet Propulsion Laboratory database (Pickett et al. 1998) for  $\text{CH}_3\text{OCHO}$  and  $\text{CH}_3\text{CHO}$ . In total, we include seven free parameters in the fit: the excitation temperature  $T_{\text{ex}}$ , the velocity line width  $\Delta V_{\text{FWHM}}$ , the systemic velocity  $v_{\text{sys}}$ , and the logarithm of the column densities of these four species. We note that here we assume a Gaussian line shape (Equation (B4)) and the line width is the one after including the broadening due to Keplerian rotation rather than the intrinsic one. This predominantly reflects the underlying assumption that the emission is optically thin, where only the velocity-integrated intensity matters for column density derivation. The actual line shape may be different from Gaussian, as usually seen in the

<sup>14</sup> This sort of column density retrieval, including the functions of querying molecular spectroscopic data, is packaged into a public Python code `specfit` (<https://github.com/yamato-as/specfit>).

**Table 3**  
Spectroscopic Properties of Major Molecular Lines

Transition	$\nu_0$ (GHz)	$\log_{10} A_{ul}$ ( $s^{-1}$ )	$g_u$	$E_u$ (K)
Dimethyl Ether ( $CH_3OCH_3$ )				
5 <sub>4,2</sub> -4 <sub>3,1</sub> AE	299.884130	-3.763	22	36.1
5 <sub>4,2</sub> -4 <sub>3,2</sub> EA	299.886128	-3.769	44	36.2
5 <sub>4,1</sub> -4 <sub>3,1</sub> EA	299.886804	-3.769	44	36.1
5 <sub>4,1</sub> -4 <sub>3,2</sub> AE	299.888802	-3.763	66	36.1
5 <sub>4,1</sub> -4 <sub>3,1</sub> EE	299.889910	-3.784	176	36.1
5 <sub>4,2</sub> -4 <sub>3,2</sub> EE	299.890981	-3.784	176	36.1
5 <sub>4,2</sub> -4 <sub>3,1</sub> AA	299.892089	-3.763	66	36.1
5 <sub>4,1</sub> -4 <sub>3,2</sub> AA	299.896762	-3.763	110	36.1
8 <sub>3,5</sub> -7 <sub>2,6</sub> AE	299.899470	-4.007	34	45.4
8 <sub>3,5</sub> -7 <sub>2,6</sub> EA	299.899781	-4.008	68	45.4
8 <sub>3,5</sub> -7 <sub>2,6</sub> EE	299.903025	-4.008	272	45.4
8 <sub>3,5</sub> -7 <sub>2,6</sub> AA	299.906424	-4.007	102	45.4
29 <sub>6,23</sub> -29 <sub>5,24</sub> AA	300.062299	-3.825	590	447.5
29 <sub>6,23</sub> -29 <sub>5,24</sub> EE	300.062707	-3.825	944	447.5
29 <sub>6,23</sub> -29 <sub>5,24</sub> AE	300.063115	-3.825	354	447.5
29 <sub>6,23</sub> -29 <sub>5,24</sub> EA	300.063116	-3.825	236	447.5
Methyl Formate ( $CH_3OCHO$ )				
23 <sub>5,18</sub> -22 <sub>5,17</sub> E, $v_t = 0$	299.097870	-3.410	94	183.9
25 <sub>3,22</sub> -24 <sub>3,21</sub> E, $v_t = 1$	299.111695	-3.406	102	387.6
23 <sub>5,18</sub> -22 <sub>5,17</sub> A, $v_t = 0$	299.123858	-3.410	94	183.9
27 <sub>1,26</sub> -26 <sub>2,25</sub> A, $v_t = 1$	299.128806	-4.243	110	397.2
27 <sub>2,26</sub> -26 <sub>2,25</sub> A, $v_t = 1$	299.131294	-3.397	110	397.2
24 <sub>8,16</sub> -23 <sub>8,16</sub> E, $v_t = 0$	299.131361	-4.932	98	220.4
27 <sub>1,26</sub> -26 <sub>1,25</sub> A, $v_t = 1$	299.133165	-3.397	110	397.2
27 <sub>2,26</sub> -26 <sub>1,25</sub> A, $v_t = 1$	299.135510	-4.243	110	397.2
12 <sub>6,6</sub> -11 <sub>5,7</sub> A, $v_t = 0$	299.162434	-4.481	50	70.0
24 <sub>7,18</sub> -23 <sub>7,17</sub> E, $v_t = 0$	300.020579	-3.426	98	210.9
24 <sub>7,18</sub> -23 <sub>7,17</sub> A, $v_t = 0$	300.035621	-3.425	98	210.9
24 <sub>6,19</sub> -23 <sub>6,18</sub> E, $v_t = 0$	300.046229	-3.415	98	202.7
24 <sub>6,19</sub> -23 <sub>6,18</sub> A, $v_t = 0$	300.063893	-3.415	98	202.7
26 <sub>3,24</sub> -25 <sub>3,23</sub> E, $v_t = 0$	300.070744	-3.398	106	206.8
34 <sub>2,32</sub> -34 <sub>1,33</sub> A, $v_t = 0$	300.071349	-4.903	138	340.3
34 <sub>3,32</sub> -34 <sub>2,33</sub> A, $v_t = 0$	300.072325	-4.903	138	340.3
26 <sub>3,24</sub> -25 <sub>3,23</sub> A, $v_t = 0$	300.079079	-3.398	106	206.8
Methanol ( $CH_3OH$ )				
4 <sub>-3,2</sub> -5 <sub>-2,4</sub> E, $v_t = 0$	288.705624	-4.734	36	70.9
6 <sub>0,6</sub> -5 <sub>0,5</sub> E, $v_t = 0$	289.939377	-3.976	52	61.8
6 <sub>1,6</sub> -5 <sub>1,5</sub> E, $v_t = 0$	290.069747	-3.987	52	54.3
6 <sub>0,6</sub> -5 <sub>0,5</sub> A, $v_t = 0$	290.110637	-3.975	52	48.7
6 <sub>5,2</sub> -5 <sub>5,1</sub> E, $v_t = 0$	290.117786	-4.489	52	172.8
6 <sub>-5,1</sub> -5 <sub>-5,0</sub> E, $v_t = 0$	290.138889	-4.489	52	184.8
6 <sub>5,2</sub> -5 <sub>5,0</sub> A, $v_t = 0$	290.145085	-4.487	52	186.6
6 <sub>5,1</sub> -5 <sub>5,1</sub> A, $v_t = 0$	290.145085	-4.487	52	186.6
6 <sub>4,3</sub> -5 <sub>4,2</sub> A, $v_t = 0$	290.161348	-4.229	52	129.1
6 <sub>4,2</sub> -5 <sub>4,1</sub> A, $v_t = 0$	290.161352	-4.229	52	129.1
6 <sub>4,3</sub> -5 <sub>4,2</sub> E, $v_t = 0$	290.162356	-4.230	52	136.6
6 <sub>-4,2</sub> -5 <sub>-4,1</sub> E, $v_t = 0$	290.183289	-4.227	52	144.7
6 <sub>2,5</sub> -5 <sub>2,4</sub> A, $v_t = 0$	290.184674	-4.023	52	86.5
6 <sub>3,4</sub> -5 <sub>3,3</sub> A, $v_t = 0$	290.189515	-4.100	52	98.5
6 <sub>3,3</sub> -5 <sub>3,2</sub> A, $v_t = 0$	290.190549	-4.100	52	98.5
6 <sub>3,3</sub> -5 <sub>3,2</sub> E, $v_t = 0$	290.209695	-4.097	52	111.5
6 <sub>-3,4</sub> -5 <sub>-3,3</sub> E, $v_t = 0$	290.213180	-4.098	52	96.5
6 <sub>-1,5</sub> -5 <sub>-1,4</sub> E, $v_t = 0$	290.248685	-3.975	52	69.8
6 <sub>2,4</sub> -5 <sub>2,3</sub> A, $v_t = 0$	290.264068	-4.022	52	86.5
6 <sub>2,4</sub> -5 <sub>2,3</sub> E, $v_t = 0$	290.307281	-4.024	52	74.7
6 <sub>-2,5</sub> -5 <sub>-2,4</sub> E, $v_t = 0$	290.307738	-4.029	52	71.0
Acetaldehyde ( $CH_3CHO$ )				
15 <sub>6,10</sub> -14 <sub>6,9</sub> A, $v_t = 0$	289.149836	-3.157	62	192.2

**Table 3**  
(Continued)

Transition	$\nu_0$ (GHz)	$\log_{10} A_{ul}$ ( $s^{-1}$ )	$g_u$	$E_u$ (K)
15 <sub>6,9</sub> -14 <sub>6,8</sub> A, $v_t = 0$	289.149853	-3.157	62	192.2
15 <sub>6,9</sub> -14 <sub>6,8</sub> E, $v_t = 0$	289.163254	-3.157	62	192.2
15 <sub>6,10</sub> -14 <sub>6,9</sub> E, $v_t = 0$	289.200782	-3.157	62	192.1
7 <sub>2,5</sub> -6 <sub>1,6</sub> E, $v_t = 0$	289.238518	-4.459	30	35.1
15 <sub>5,11</sub> -14 <sub>5,10</sub> A, $v_t = 0$	289.272555	-3.132	62	167.5
15 <sub>5,10</sub> -14 <sub>5,9</sub> A, $v_t = 0$	289.273794	-3.132	62	167.5
15 <sub>5,10</sub> -14 <sub>5,9</sub> E, $v_t = 0$	289.316721	-3.132	62	167.4
15 <sub>5,11</sub> -14 <sub>5,10</sub> E, $v_t = 0$	289.322537	-3.132	62	167.4
15 <sub>4,12</sub> -14 <sub>4,11</sub> A, $v_t = 0$	289.506111	-3.112	62	147.2
15 <sub>4,11</sub> -14 <sub>4,10</sub> A, $v_t = 0$	289.558746	-3.112	62	147.3
15 <sub>4,11</sub> -14 <sub>4,10</sub> E, $v_t = 0$	289.562297	-3.112	62	147.2
15 <sub>4,12</sub> -14 <sub>4,11</sub> E, $v_t = 0$	289.585326	-3.112	62	147.2
15 <sub>3,13</sub> -14 <sub>3,12</sub> A, $v_t = 0$	289.602928	-3.097	62	131.5
15 <sub>3,13</sub> -14 <sub>3,12</sub> E, $v_t = 0$	289.716267	-3.101	62	131.4
7 <sub>2,5</sub> -6 <sub>1,6</sub> A, $v_t = 0$	289.942040	-4.371	30	35.0
16 <sub>0,16</sub> -15 <sub>0,15</sub> E, $v_t = 0$	299.174780	-3.038	66	123.6
16 <sub>0,16</sub> -15 <sub>0,15</sub> A, $v_t = 0$	299.218175	-3.038	66	123.5

**Note.** For (tentatively) detected species ( $CH_3OCH_3$  and  $CH_3OCHO$ ), all transitions that could be responsible for the observed signals are listed. For nondetected species ( $CH_3OH$  and  $CH_3CHO$ ), only strong transitions ( $\log_{10} A_{ul} (s^{-1}) \geq -5$  and  $E_u \leq 200$  K) that effectively constrain the column upper limits are listed.

spectra of rotating disks, but given the unresolved emission, the low S/N, and the low spectral resolution, we do not perform a detailed line shape modeling here and it is partly addressed in the radiative transfer modeling (Appendix C).

We explore the parameter space with the affine-invariant MCMC algorithm implemented in the Python package `emcee` (Foreman-Mackey et al. 2013) using uniform prior distributions:

$$T_{\text{ex}} \text{ (K)} = \mathcal{U}(5, 1000),$$

$$\Delta V_{\text{FWHM}} \text{ (km s}^{-1}\text{)} = \mathcal{U}(0.0, 100.0),$$

$$v_{\text{sys}} \text{ (km s}^{-1}\text{)} = \mathcal{U}(-5.0, 15.0),$$

$$\log_{10} N(X) \text{ (cm}^{-2}\text{)} = \mathcal{U}(10.0, 20.0),$$

where  $\mathcal{U}(a, b)$  denotes the uniform distributions between  $a$  and  $b$ , and  $X$  represents the four molecular species. We exclude the following frequency ranges from the fit, due to the contamination from other molecular lines and telluric absorption lines: [288.85, 289.00], [289.62, 289.66], [300.13, 300.18], and [300.64, 300.70] in gigahertz. We run 50 walkers for 10,000 steps to sample the posterior distributions, and the initial 2000 steps are discarded as burn-in. Figure 4 shows the parameter covariances and marginalized posterior distributions. Only the upper limits on the  $CH_3OH$  and  $CH_3CHO$  column density are constrained due to the nondetection. The median value of the systemic velocity ( $\approx 4.3$  km s $^{-1}$ ) is slightly shifted from the literature value ( $\approx 5.1$  km s $^{-1}$ ; Piétu et al. 2007; Teague et al. 2021) due to the coarse channel width ( $\approx 4$  km s $^{-1}$ ), and these are consistent within the uncertainty. From these posterior samples, we compute the column density ratios relative to  $CH_3OH$ , where  $N(CH_3OCH_3)/N(CH_3OH)$  is constrained to be  $>7$  (0.15th percentile, corresponding to  $3\sigma$  for a Gaussian distribution). For  $CH_3OCHO$ , while the 0.15th percentile of  $N(CH_3OCH_3)/N(CH_3OH)$  is very small, due to the long tail in

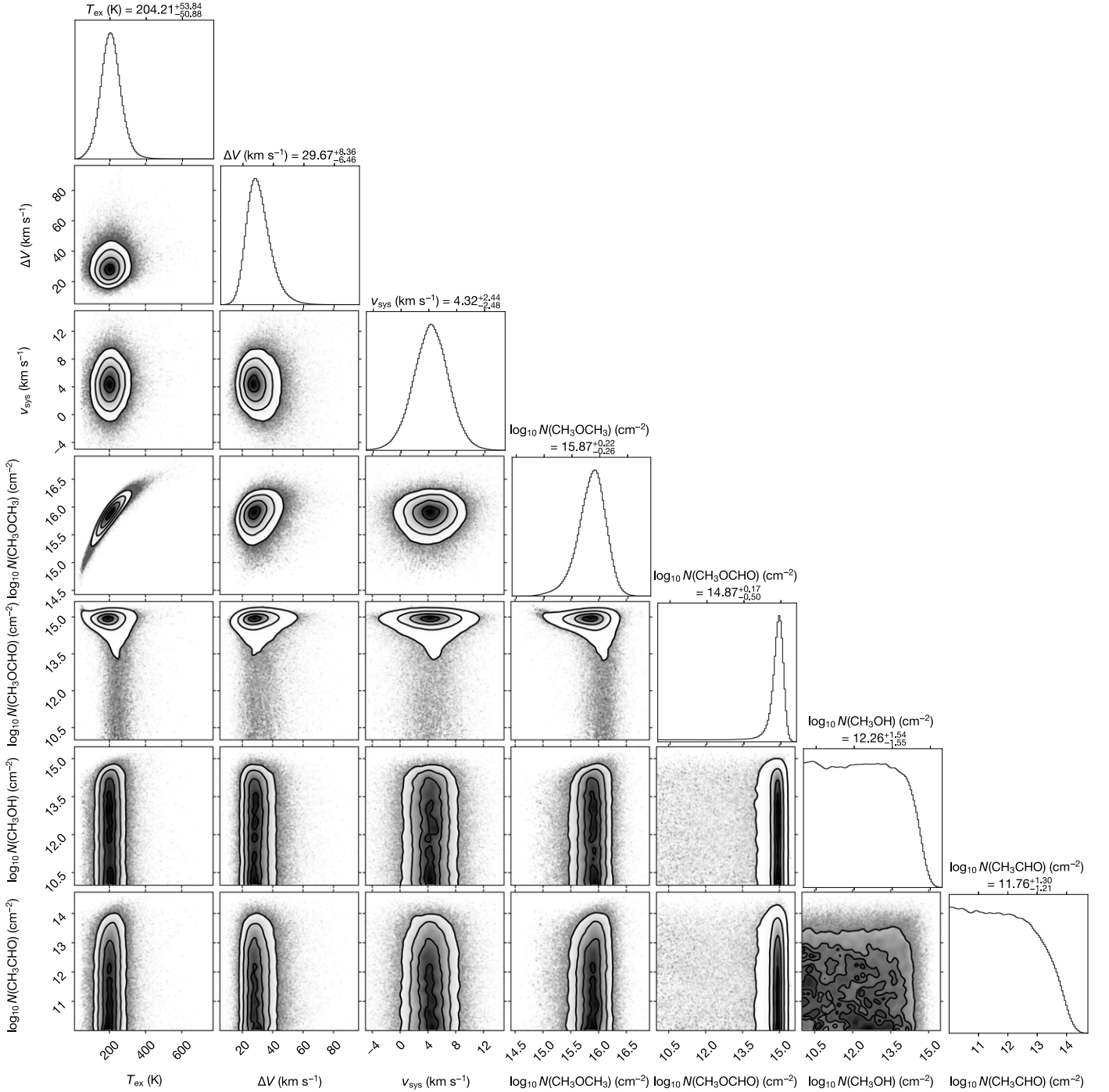


**Figure 4.** Parameter covariances and marginalized posterior distributions for the MCMC spectral fit. The values and errors at the top of each panel indicate the 16th, 50th (median), and 84th percentiles of the posterior distributions.

the posterior distributions of  $N(\text{CH}_3\text{OCHO})$  (see Figure 4), the median values of  $N(\text{CH}_3\text{OCHO})$  divided by the upper limit of  $N(\text{CH}_3\text{OH})$  are listed in Table 2 and added in Figure 2 as a reference. For  $\text{CH}_3\text{CHO}$ , we do not obtain meaningful constraints due to the nondetection.

### Appendix C Parametric Disk Model

Here, we demonstrate a detailed radiative transfer calculation of a disk model that aims to constrain what spatial distributions of COMs in the inner disk can explain the observed  $\text{CH}_3\text{OCH}_3$

emission with a more realistic disk physical structure. Additionally, we examine if the difference in the spatial distributions of  $\text{CH}_3\text{OCH}_3$  and  $\text{CH}_3\text{OH}$  can explain the nondetection of  $\text{CH}_3\text{OH}$ , as discussed in Section 4.1.

As the disk density and temperature structures, we used the disk model tailored to MWC 480 in Zhang et al. (2021). The details of the model are presented in the original paper. Briefly, the model assumed two populations (small and large) of dust grains, and the distributions of large dust grains are constrained from the high-resolution ALMA observations. The small dust grains are assumed to be completely coupled with the gas.

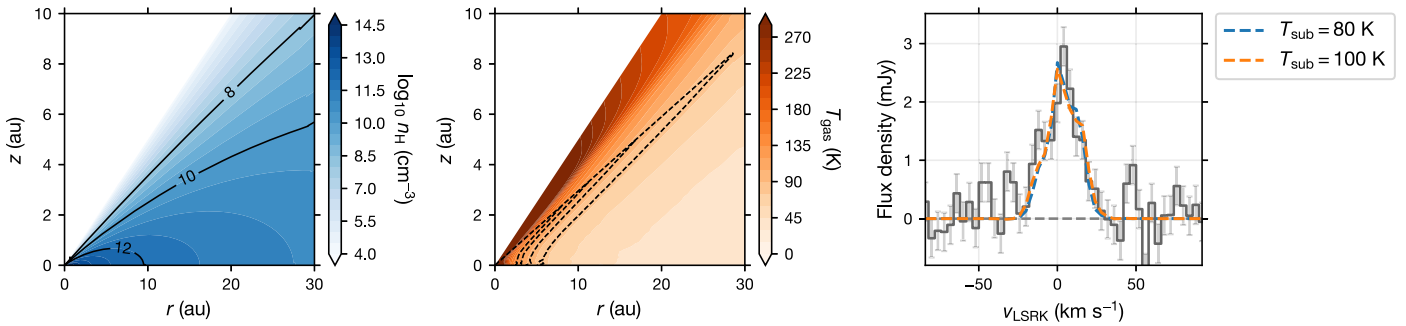


**Figure 5.** Left and middle: gas density (left) and temperature (middle) structure of the disk model. The dashed lines in the middle panel enclose the region where molecules distribute for each boundary temperature in the models (80, 100, 120, and 140 K from outside). The upper boundary of the regions is  $z/r = 0.3$ , which is also depicted by the dashed lines. Right: comparison of the observed and modeled spectra of the  $\text{CH}_3\text{OCH}_3$  transitions at  $\sim 299.89$  GHz for the models, with different boundary temperatures of  $\text{CH}_3\text{OCH}_3$  (blue for the 80 K model and orange for the 100 K model). The spectra of these models are nearly identical and overlap.

**Table 4**  
Disk Modeling Results

$r_{\text{in}}$ (au)	$r_{\text{out}}$ (au)	$(z/r)_{\text{min}}$	$(z/r)_{\text{max}}$	$T_{\text{sub}}(\text{CH}_3\text{OCH}_3)$ (K)	$T_{\text{sub}}(\text{CH}_3\text{OH})$ (K)	$x(\text{CH}_3\text{OCH}_3)$	$x(\text{CH}_3\text{OH})$	$x(\text{CH}_3\text{OCH}_3)/x(\text{CH}_3\text{OH})$
0.5	30	0.0	0.3	80	100	$3.0 \times 10^{-8}$	$< 3.1 \times 10^{-8}$	$> 0.97$
0.5	30	0.0	0.3	80	120	$3.0 \times 10^{-8}$	$< 1.2 \times 10^{-7}$	$> 0.25$
0.5	30	0.0	0.3	100	120	$1.8 \times 10^{-7}$	$< 1.0 \times 10^{-7}$	$> 1.8$
0.5	30	0.0	0.3	100	140	$1.8 \times 10^{-7}$	$< 5.8 \times 10^{-7}$	$> 0.31$

While in the original model, the gas temperature structure is computed by thermochemical modeling, given the uncertainty of the modeling in the inner region, here we simply assume that the gas temperature is the same as the dust temperature (surface-area-weighted over both populations) computed with thermal Monte Carlo simulations using the RADMC-3D package (Dullemond et al. 2012). The gas density and temperature distributions used for the present calculations are shown in Figure 5.

The distributions of the warm  $\text{CH}_3\text{OCH}_3$  and  $\text{CH}_3\text{OH}$  gas are assumed based on the dust temperature, which controls the ice sublimation. Since in general the sublimation temperature of a specific molecule is proportional to the binding energy of the molecule (e.g., Furuya & Aikawa 2014), the sublimation temperature ratio between  $\text{CH}_3\text{OCH}_3$  and  $\text{CH}_3\text{OH}$  should be the same as the binding energy ratio. Although the absolute values of binding energy for  $\text{CH}_3\text{OCH}_3$  and  $\text{CH}_3\text{OH}$  show some scatter, depending on the experimental methods and the composition of the surface, there is a trend that  $\text{CH}_3\text{OCH}_3$  has a lower binding energy than  $\text{CH}_3\text{OH}$ . The experimental estimates of the binding energies of  $\text{CH}_3\text{OCH}_3$  ( $\approx 4000$  K; Lattalais et al. 2011) and  $\text{CH}_3\text{OH}$  ( $\approx 5000$ – $5500$  K; Ferrero et al. 2020; Minissale et al. 2022) thus lead to the sublimation temperature ratio of  $T_{\text{sub}}(\text{CH}_3\text{OH})/T_{\text{sub}}(\text{CH}_3\text{OCH}_3) \approx 1.2$ – $1.4$ . Based on this ratio and the gas density of the inner disk, we constructed a series of models in which  $\text{CH}_3\text{OCH}_3$  and  $\text{CH}_3\text{OH}$  distribute with a constant abundance  $x$  (relative to the  $\text{H}_2$  molecule) in the regions where the dust temperature is higher than 80 and 100 K for  $\text{CH}_3\text{OCH}_3$  and higher than 100, 120, and 140 K for  $\text{CH}_3\text{OH}$ . This emulates the drastic gas-phase abundance increases due to thermal desorption. We additionally set an upper boundary of  $z/r \lesssim 0.3$ , reflecting the expectation that molecules can be destroyed in the irradiated surface of the disk (e.g., Walsh et al. 2014). Outside these boundaries, the abundances of  $\text{CH}_3\text{OH}$  and  $\text{CH}_3\text{OCH}_3$  are set to zero, which is a suitable first-order approximation, given the steep (exponential) dependence of gaseous molecular abundances

on visual extinction and dust temperature around its sublimation temperature. The dependence of COM abundances on other parameters such as gas density is weaker (e.g., Hasegawa et al. 1992; Furuya & Aikawa 2014). This resulted in the distributions of warm  $\text{CH}_3\text{OCH}_3$  and  $\text{CH}_3\text{OH}$  gas all within  $\lesssim 20$ – $30$  au (the middle panel of Figure 5). The velocity structure of the warm gas is assumed to be in Keplerian rotation with a known stellar mass of  $2.1M_{\odot}$  (e.g., Teague et al. 2021).

For the models with different combinations of boundary temperatures, as listed in Table 4, which have at maximum a sublimation temperature ratio of 1.5 as the most extreme case, we compute image cubes covering the frequency ranges of the robustly detected  $\text{CH}_3\text{OCH}_3$  transitions at  $\sim 299.89$  GHz and the undetected  $\text{CH}_3\text{OH}$  transitions at 290.0–290.4 GHz using the RADMC-3D package (Dullemond et al. 2012). The resulting image cubes are convolved with the observing beam, continuum-subtracted, and spatially integrated to create the disk-integrated spectra, which are then compared to the observed spectra. The abundances  $x(\text{CH}_3\text{OCH}_3)$  and  $x(\text{CH}_3\text{OH})$  are adjusted to fit the observed spectra.

The right panel of Figure 5 compares the best-fit model with the observed spectrum of  $\text{CH}_3\text{OCH}_3$  at  $\sim 299.89$  GHz. Both models with boundary temperatures of 80 and 100 K reproduce the spectrum well, particularly the broad line width. Furthermore, the nondetection of  $\text{CH}_3\text{OH}$  places constraints on the abundance ratio  $x(\text{CH}_3\text{OCH}_3)/x(\text{CH}_3\text{OH})$  of the warm gas, as listed in Table 4. The constrained lower limits of the abundance ratios span  $\sim 0.3$ – $2$ , depending on the combination of the boundary temperatures. These values are lower than the column density ratio derived in the spectral analysis in Section 3.2 (where the same distributions are implicitly assumed) by a factor of  $\sim 3$ – $20$ . This indicates that the spatial distribution is a critical factor in measuring the correct abundance ratio. Further spatially resolved observations are necessary. It should be noted that the disk physical structure used in this modeling is an extrapolation of the outer disk structure. The actual structure can vary—for example, due to

the accretion heating that could modify the temperature structure of the inner disk. Constraining the inner disk structure is also essential to inferring the inner disk chemistry.

### Appendix D Detection of a New Submillimeter Source

We report the detection of a new submillimeter source at a separation of  $\approx 5''.2$  from the central star with a position angle of  $212^\circ.5$  (Figure 6). The emission is compact and reaches a peak S/N of  $\approx 7$  on the image made with a Briggs robust value of 0.5. The coordinate of the continuum peak is  $\alpha(\text{J2000}) = 4^{\text{h}}58^{\text{m}}46^{\text{s}}.066$ ;  $\delta(\text{J2000}) = 29^{\text{d}}50^{\text{m}}32^{\text{s}}.04$ . To characterize the emission, we performed a Gaussian fit to this component with the CASA task `imfit`, which obtained a deconvolved size of  $0''.33 \times 0''.13$  (PA =  $179^\circ$ ) and a flux density of 0.32 mJy. Although the origin of this emission is unclear, this component is located outside the  $^{12}\text{CO}$  gas disk characterized in Teague et al. (2021), and thus it is unlikely that the emission is attributed to the circumplanetary disk around a forming planet in the MWC 480 disk. It is possible that this originates from the disk or envelope around a field star or from a background galaxy.

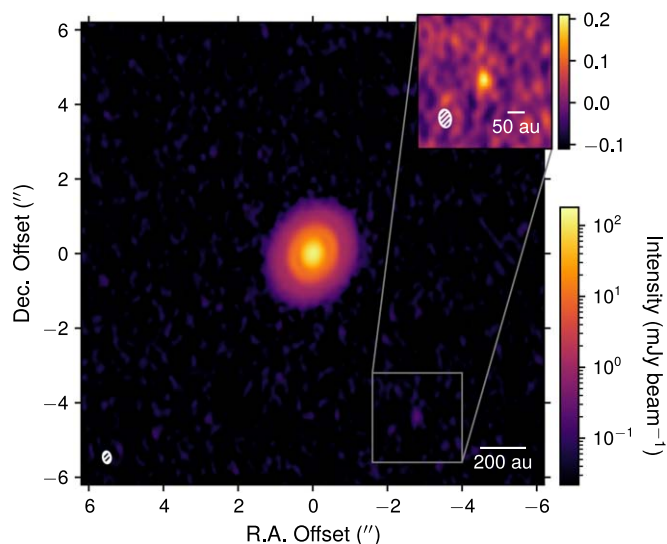


**Figure 6.** 1.03 mm continuum image made with a Briggs robust value of 0.5. The inset panel presents the zoomed-in view of the vicinity of the new submillimeter source. The beam size of  $0''.31 \times 0''.21$  (PA =  $8^\circ.2$ ) is shown in the lower left corner of each panel. A scale bar is shown in the lower right corner of each panel.

### ORCID iDs

Yoshihide Yamato <https://orcid.org/0000-0003-4099-6941>  
 Yuri Aikawa <https://orcid.org/0000-0003-3283-6884>  
 Viviana V. Guzmán <https://orcid.org/0000-0003-4784-3040>  
 Kenji Furuya <https://orcid.org/0000-0002-2026-8157>  
 Shota Notsu <https://orcid.org/0000-0003-2493-912X>  
 Gianni Cataldi <https://orcid.org/0000-0002-2700-9676>  
 Karin I. Öberg <https://orcid.org/0000-0001-8798-1347>  
 Chunhua Qi <https://orcid.org/0000-0001-8642-1786>  
 Charles J. Law <https://orcid.org/0000-0003-1413-1776>  
 Jane Huang <https://orcid.org/0000-0001-6947-6072>  
 Richard Teague <https://orcid.org/0000-0003-1534-5186>  
 Romane Le Gal <https://orcid.org/0000-0003-1837-3772>

### References

- Aikawa, Y., Cataldi, G., Yamato, Y., et al. 2021, *ApJS*, **257**, 13  
 Altwegg, K., Balsiger, H., & Fuselier, S. A. 2019, *ARA&A*, **57**, 113  
 Astropy Collaboration, Price-Whelan, A. M., Lim, P. L., et al. 2022, *ApJ*, **935**, 167  
 Astropy Collaboration, Price-Whelan, A. M., Sipőcz, B. M., et al. 2018, *AJ*, **156**, 123  
 Astropy Collaboration, Robitaille, T. P., Tollerud, E. J., et al. 2013, *A&A*, **558**, A33  
 Banzatti, A., Pontoppidan, K. M., Péré Chávez, J., et al. 2023, *AJ*, **165**, 72  
 Belloche, A., Maury, A. J., Maret, S., et al. 2020, *A&A*, **635**, A198  
 Booth, A. S., Law, C. J., Temmink, M., Leemker, M., & Macias, E. 2023, *A&A*, **678**, A146  
 Booth, A. S., Leemker, M., van Dishoeck, E. F., et al. 2024a, *AJ*, **167**, 164  
 Booth, A. S., Temmink, M., van Dishoeck, E. F., et al. 2024b, *AJ*, **167**, 165  
 Booth, A. S., van der Marel, N., Leemker, M., van Dishoeck, E. F., & Ohashi, S. 2021a, *A&A*, **651**, L6  
 Booth, A. S., Walsh, C., Terwisscha van Scheltinga, J., et al. 2021b, *NatAs*, **5**, 684  
 Bosman, A. D., Alarcón, F., Bergin, E. A., et al. 2021a, *ApJS*, **257**, 7  
 Bosman, A. D., Bergin, E. A., Loomis, R. A., et al. 2021b, *ApJS*, **257**, 15  
 Brunken, N. G. C., Booth, A. S., Leemker, M., et al. 2022, *A&A*, **659**, A29  
 Carney, M. T., Hogerheijde, M. R., Guzmán, V. V., et al. 2019, *A&A*, **623**, A124  
 CASA Team, Bean, B., Bhatnagar, S., et al. 2022, *PASP*, **134**, 114501  
 Ceccarelli, C., Codella, C., Balucani, N., et al. 2023, in *ASP Conf. Ser.* 534, Protostars and Planets VII (San Francisco, CA: ASP), 379  
 Drozdovskaya, M. N., van Dishoeck, E. F., Rubin, M., Jørgensen, J. K., & Altwegg, K. 2019, *MNRAS*, **490**, 50  
 Dullemond, C. P., Juhasz, A., Pohl, A., et al. 2012, RADMC-3D: A multi-purpose radiative transfer tool, *Astrophysics Source Code Library*, ascl:1202.015  
 Endres, C. P., Schlemmer, S., Schilke, P., Stutzki, J., & Müller, H. S. P. 2016, *JMoSp*, **327**, 95  
 Fairlamb, J. R., Oudmaijer, R. D., Mendigutia, I., Ilee, J. D., & van den Ancker, M. E. 2015, *MNRAS*, **453**, 976  
 Ferrero, S., Zamirri, L., Ceccarelli, C., et al. 2020, *ApJ*, **904**, 11  
 Foreman-Mackey, D. 2016, *JOSS*, **1**, 24  
 Foreman-Mackey, D., Hogg, D. W., Lang, D., & Goodman, J. 2013, *PASP*, **125**, 306  
 Furuya, K., & Aikawa, Y. 2014, *ApJ*, **790**, 97  
 Gaia Collaboration, Brown, A. G. A., Vallenari, A., et al. 2018, *A&A*, **616**, A1  
 Garrod, R. T., Jin, M., Matis, K. A., et al. 2022, *ApJS*, **259**, 1  
 Guzmán, V. V., Bergner, J. B., Law, C. J., et al. 2021, *ApJS*, **257**, 6  
 Harris, C. R., Millman, K. J., van der Walt, S. J., et al. 2020, *Natur*, **585**, 357  
 Hasegawa, T. I., Herbst, E., & Leung, C. M. 1992, *ApJS*, **82**, 167  
 Herbst, E., & van Dishoeck, E. F. 2009, *ARA&A*, **47**, 427  
 Hunter, J. D. 2007, *CSE*, **9**, 90  
 Ilee, J. D., Walsh, C., Booth, A. S., et al. 2021, *ApJS*, **257**, 9  
 Izquierdo, A. F., Testi, L., Facchini, S., et al. 2023, *A&A*, **674**, A113  
 Jiang, H., Wang, Y., Ormel, C. W., Krijt, S., & Dong, R. 2023, *A&A*, **678**, A33  
 Jørgensen, J. K., Müller, H. S. P., Calcutt, H., et al. 2018, *A&A*, **620**, A170  
 Jørgensen, J. K., van der Wiel, M. H. D., Coutens, A., et al. 2016, *A&A*, **595**, A117  
 Lattalais, M., Bertin, M., Mokrane, H., et al. 2011, *A&A*, **532**, A12  
 Law, C. J., Teague, R., Loomis, R. A., et al. 2021, *ApJS*, **257**, 4  
 Lee, J.-E., Lee, S., Baek, G., et al. 2019, *NatAs*, **3**, 314  
 Leemker, M., Booth, A. S., van Dishoeck, E. F., et al. 2023, *A&A*, **673**, A7  
 Leemker, M., van't Hoff, M. L. R., Trapman, L., et al. 2021, *A&A*, **646**, A3  
 Ligerink, N. F. W., & Minissale, M. 2023, *A&A*, **676**, A80  
 Liu, Y., Dipierro, G., Ragusa, E., et al. 2019, *A&A*, **622**, A75  
 Long, F., Pinilla, P., Herczeg, G. J., et al. 2018, *ApJ*, **869**, 17  
 Loomis, R. A., Cleeves, L. I., Öberg, K. I., et al. 2018a, *ApJ*, **859**, 131  
 Loomis, R. A., Öberg, K. I., Andrews, S. M., et al. 2018b, *AJ*, **155**, 182  
 Mendigutia, I., Brittain, S., Eiroa, C., et al. 2013, *ApJ*, **776**, 44  
 Minissale, M., Aikawa, Y., Bergin, E., et al. 2022, *ESC*, **6**, 597  
 Montesinos, B., Eiroa, C., Mora, A., & Merín, B. 2009, *A&A*, **495**, 901  
 Müller, H. S. P., Schlöder, F., Stutzki, J., & Winnewisser, G. 2005, *JMoSp*, **742**, 215  
 Müller, H. S. P., Thorwirth, S., Roth, D. A., & Winnewisser, G. 2001, *A&A*, **370**, L49  
 Öberg, K. I., Garrod, R. T., van Dishoeck, E. F., & Linnartz, H. 2009, *A&A*, **504**, 891  
 Öberg, K. I., Guzmán, V. V., Walsh, C., et al. 2021, *ApJS*, **257**, 1

- Pickett, H. M., Poynter, R. L., Cohen, E. A., et al. 1998, *JQSRT*, **60**, 883
- Piétu, V., Dutrey, A., & Guilloteau, S. 2007, *A&A*, **467**, 163
- Sierra, A., Pérez, L. M., Zhang, K., et al. 2021, *ApJS*, **257**, 14
- Simon, M., Guilloteau, S., Beck, T. L., et al. 2019, *ApJ*, **884**, 42
- Taquet, V., Wirström, E. S., & Charnley, S. B. 2016, *ApJ*, **821**, 46
- Teague, R. 2020, richteague/keplerian\_mask: Initial Release, v1.0, Zenodo, doi:10.5281/zenodo.4321137
- Teague, R., Bae, J., Aikawa, Y., et al. 2021, *ApJS*, **257**, 18
- Teague, R., & Foreman-Mackey, D. 2018, *RNAAS*, **2**, 173
- Thyng, K. M., Greene, C. A., Hetland, R. D., Zimmerle, H. M., & DiMarco, S. F. 2016, *Oceanography*, **29**, 9
- van der Marel, N., Booth, A. S., Leemker, M., van Dishoeck, E. F., & Ohashi, S. 2021, *A&A*, **651**, L5
- van 't Hoff, M. L. R., Tobin, J. J., Trapman, L., et al. 2018, *ApJL*, **864**, L23
- Virtanen, P., Gommers, R., Oliphant, T. E., et al. 2020, *NatMe*, **17**, 261
- Walsh, C., Loomis, R. A., Öberg, K. I., et al. 2016, *ApJL*, **823**, L10
- Walsh, C., Millar, T. J., Nomura, H., et al. 2014, *A&A*, **563**, A33
- Watanabe, N., & Kouchi, A. 2002, *ApJL*, **571**, L173
- Yamaguchi, M., Muto, T., Tsukagoshi, T., et al. 2024, *PASJ*, **76**, 437
- Yamato, Y., Notsu, S., Aikawa, Y., et al. 2024, *AJ*, **167**, 66
- Yang, Y.-L., Sakai, N., Zhang, Y., et al. 2021, *ApJ*, **910**, 20
- Zhang, K., Booth, A. S., Law, C. J., et al. 2021, *ApJS*, **257**, 5